Tayyab, Zuhra; Rauf, Sajid; Xia, Chen; Wang, Baoyuan; Shah, M. A.K.Yousaf; Mushtaq, Naveed; Liang, Shi Heng; Yang, Changping; Lund, Peter D.; Asghar, Muhammad Imran

Advanced LT-SOFC Based on Reconstruction of the Energy Band Structure of the $LiNi_{0.8}Co_{0.15}Al_{0.05}O_2$-$Sm_{0.2}Ce_{0.8}O_{2-\delta}$ Heterostructure for Fast Ionic Transport

Published in:
ACS Applied Energy Materials

DOI:
10.1021/acsaem.1c01186

Published: 27/09/2021

Document Version
Publisher's PDF, also known as Version of record

Please cite the original version:
Tayyab, Z., Rauf, S., Xia, C., Wang, B., Shah, M. A. K. Y., Mushtaq, N., Liang, S. H., Yang, C., Lund, P. D., & Asghar, M. I. (2021). Advanced LT-SOFC Based on Reconstruction of the Energy Band Structure of the $LiNi_{0.8}Co_{0.15}Al_{0.05}O_2$-$Sm_{0.2}Ce_{0.8}O_{2-\delta}$ Heterostructure for Fast Ionic Transport. *ACS Applied Energy Materials*, *4*(9), 8922-8932. https://doi.org/10.1021/acsaem.1c01186

ACS APPLIED ENERGY MATERIALS

www.acsaem.org

Article

Advanced LT-SOFC Based on Reconstruction of the Energy Band Structure of the $LiNi_{0.8}Co_{0.15}Al_{0.05}O_2-Sm_{0.2}Ce_{0.8}O_{2-\delta}$ Heterostructure for Fast Ionic Transport

Zuhra Tayyab, Sajid Rauf, Chen Xia, Baoyuan Wang, M.A.K. Yousaf Shah, Naveed Mushtaq, Shi Heng Liang,* Changping Yang,* Peter D. Lund, and Muhammad Imran Asghar*

Cite This: *ACS Appl. Energy Mater.* 2021, 4, 8922−8932

Read Online

ACCESS | Metrics & More | Article Recommendations | Supporting Information

ABSTRACT: Formation of a heterostructure of semiconductor materials is a promising method to develop an electrolyte with high ionic conductivity at low operational temperature of solid oxide fuel cells (LT-SOFCs). Herein, we develop various heterostructure composites by introducing a pure ionic conductor $Sm_{0.2}Ce_{0.8}O_{2-\delta}$ (SDC) into a semiconductor $LiNi_{0.8}Co_{0.15}Al_{0.05}O_2$ (LNCA) for LT-SOFCs electrolyte. The morphology, crystal structure, elemental distribution, micro-structure, and oxidation states of the composite of LNCA−SDC are analyzed and studied via X-ray diffraction (XRD), field-emission scanning electron microscopy (FE-SEM), high resolution-transmission electron microscopy (HR-TEM), high energy dispersive spectrometry, and X-ray photoelectron spectroscopy (XPS). Electrochemical studies found that the optimal weight ratio of 0.5 LNCA-1.5 SDC heterostructure composite exhibits relatively high ionic conductivity (0.12 S cm^{-1} at 520 °C), which is much higher than that of SDC. The designed composite of LNCA-SDC heterostructures with optimal weight ratio (0.5:1.5) delivers a remarkable fuel cell power output of 0.735 W cm^{-2} at 520 °C. The formation of the heterostructure and reconstruction of energy bands at the interface play the crucial roles in enhancing ionic conduction to improve electrochemical performance. The prepared composite heterostructure delivers a unique and insightful strategy of electrolyte in advanced LT-SOFCs.

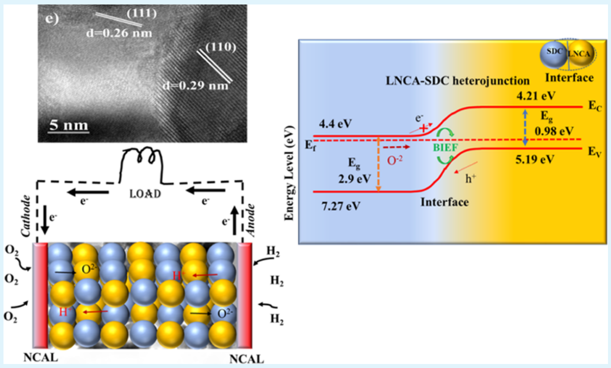

KEYWORDS: *semiconductor electrolyte, semiconductor-ionic composite, ionic conductivity, band bending, junction, low temperature*

1.INTRODUCTION

The promising energy conversion devices include solid oxide fuel cell (SOFC) to convert the chemical energy directly to electrical energy without pollutants. However, lowering their operating temperature is a major research and development challenge and an important prerequisite for increasing efficiency and its commercialization.[1,2] The performance of SOFC is intensely dependent on the high ionic transport of electrolyte, and ionic conduction in solid electrolyte materials has a direct effect on Ohmic polarization losses in SOFC operation.[3,4] Indeed, the high operating temperatures (800−1000 °C) offered high cost manufacturing and maintenance and a main-stream hurdles for the SOFCs.[1] For example, Y_2O_3-stabilized ZrO_2 (YSZ) and gadolinia-doped ceria, which have often been used, have an inherent high resistance for ionic transport and need a high temperature to operate satisfactorily.[5] However, lowering the operational temperature encountered with Ohmic losses exhibit by electrolyte in SOFC severely affect the device efficiency. Therefore, various techniques were adopted to overcome the Ohmic resistance and managed at low-temperature SOFC (LT-SOFC), for instance, advanced thin-film technology was engaged to engineer thin films of YSZ to lower the Ohmic polarization resistance. However, thin-film technology is still associated with high costs and difficulty of scaling-up and adversely affects the durability of the SOFC stack, which obstruct the practical utilization.[6−12]

Therefore, there is a prerequisite to develop new semiconducting material-based electrolytes applicable for low temperature operation.[13] For this purpose, single-phase semiconductor electrolyte materials with attractive characteristics have been investigated, where they involve structural doping and bulk ionic conduction encountered with many

Received: April 25, 2021
Accepted: August 19, 2021
Published: August 31, 2021

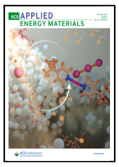

https://doi.org/10.1021/acsaem.1c01186

challenges.[14,15] Moreover, new discoveries of advanced semiconductor electrolyte materials were reported; Lan et al. reported layered structured $Li_xCo_{0.5}Al_{0.5}O_2$ (LCAO) materials as electrolyte in fuel cell considered to maintain the electronic characteristics.[16] In contrast to a conventional fuel cell, the electronic conductor was transformed into a proton conductor, which induced the protons into the LCAO structure under a H_2/air environment; it resulted in an acceptable power output of 0.12 W cm^{-2} and high protonic conductivity of 0.1 S cm^{-1} at 550 °C. Similarly, $SmNiO_{3-\delta}$ (SNO) perovskite was reported as an electrolyte with high protonic conductivity (0.1 S cm^{-1}) and generated good power output of 0.225 W cm^{-2} at 500 °C by the virtue of the Mott transition effect in SNO.[17]

Besides, there are several new semiconductor composite heterostructures with outstanding power density and high ionic conduction.[18−20] Interestingly, the diffusion via the interface is more appropriate in a semiconductor heterostructure, which plays a crucial role in enhancing ionic conduction. In this regard, the SCDC-$La_{0.6}Sr_{0.4}Co_{0.2}Fe_{0.8}O_{3-\delta}$ heterostructure has been reported to involve the creation of high content of oxygen vacancies at the interface region of heterostructure, which were detected by employing TEM and other spectroscopies.[21] Hence, it was regarded as the reason to improve ionic conductivity to 0.188 S cm^{-1} at 600 °C. Furthermore, a novel heterostructure of a semiconductor-ionic $Co_{0.2}Zn_{0.8}O$-SDC material has been reported as an electrolyte in the fuel cell and displayed an attractive ionic conduction and power output of 0.24 S cm^{-1} and 0.928 W cm^{-2}, respectively, at 550 °C.[18] Mushtaq et al. reported a mixed electron ion-conducting semiconductor-ionic $SrFe_{0.75}Ti_{0.25}O_{3-\delta}$-SDC electrolyte in the fuel cell with high ionic conductivity (>0.1 S cm^{-1}), which resulted in a remarkable power output of 0.92 W cm^{-2} at a low operational temperature of 520 °C,[22] and many others are reported.[23] Moreover, Yang et al. have reported one order of magnitude enhancement in the ionic conduction via formation of the heterostructure of vertical nanocolumns using $Sm_{0.25}Ce_{0.75}O_{2-\delta}$ (SDC) and $SrTiO_{3-\delta}$ as compared to individual ionic conductor SDC.[24,25] Hence, the construction of an artificial heterostructure based on currently developed materials amalgamated with present developments created new pathways and extended the number of semiconductor heterojunctions and superlattices to assist the transport of oxide ions.[26] Therefore, to pursue this concept, a p−n heterojunction in bulk was studied based on nano-redox at particles and nano-fuel cell reactions. The p−n heterojunction plays a crucial role in the separation of the electron−hole pairs via the formation of the internal electric field.[27−29]

It is well known that $Ni_{0.8}Co_{0.15}Al_{0.05}LiO_2$ (NCAL) has been employed in Li-ion batteries as a common cathode material,[30] but recently, NCAL has been widely employed as the symmetrical electrode for developing LT-SOFC, and it showed good catalytic activity and appreciable triple proton/oxygen ion/electron conduction at low operating temperatures.[31−33] The good ionic transport of NCAL has also been reported in recent studies.[34,35] Therefore, to understand the concept of semiconductor-ionic heterostructure composite formation, herein, we tuned the layered structure LNCA to enhance the ionic conductivity via construction of a semiconductor-ionic heterostructure composite of LNCA with SDC with an optimal weight ratio of 0.5:1.5. The fuel cell utilizing the proposed composite of the LNCA-SDC electrolyte yielded a high power output of 0.735 W cm^{-2} at 520 °C, where the obtained ionic conductivity of 0.12 S cm^{-1} is far better than that of SDC (0.022 S cm^{-1}). Moreover, the charge transfer and the promotion and enhancement of ionic conduction were understood via employing the energy band alignment concept, followed by the band bending at the interface region of the constructed heterostructure.[36] Moreover, the LNCA-SDC composite was electrochemically and physically characterized via different characterization tools to study the electrical properties, morphology, and microstructure and energy structure. Therefore, specific emphasis was given to the development of the optimal heterostructure composite to tune their ionic properties and then study their effect on the enhancement of the ionic conduction.

2. MATERIAL PREPARATION AND THEIR METHODS

2.1. Preparation of Material and Their Characterization.

LNCA ($LiNi_{0.8}Co_{0.15}Al_{0.05}O_2$) powder was prepared employing the method of a solid−state reaction method. A stoichiometric amount of lithium nitrate ($LiNO_3$), nickel nitrate hexa-hydrate ($Ni(NO_3)_2\cdot6H_2O$), cobalt nitrate hexa-hydrate ($Co(NO_3)_2\cdot6H_2O$), and aluminum nitrate nano-hydrate ($Al(NO_3)_3\cdot9H_2O$) was correctly mixed in a mortar and pestle and ground well. After grinding, the powder was sintered at 900 °C for 4 h in a muffle furnace. The obtained powder was used as the final product after the second grinding. The schematic preparation method is presented below in Figure 1.

Figure 1. Schematic description of LNCA powder preparation.

After the preparation of LNCA and SDC powders, various compositions of LNCA and SDC were prepared, such as 1.9 LNCA:0.1 SDC, 1.5 LNCA:0.5 SDC, 1.0 LNCA:1.0 SDC, 0.5 LNCA:1.5 SDC, and 0.1 LNCA:1.9 SDC. The proposed compositions were prepared by mixing the appropriate weight ratio of each constituent of compositions in the ethanol absolute mixing media via the solid state reaction method utilizing the agate balls for four (04) h. Afterward, the materials were collected and dried at 120 °C for 5 h and then ground adequately. Furthermore, the powder was sintered at 700 °C in an open furnace for 2 h and crushed very well and can be utilized aimed at auxiliary electrochemical and physical characterizations.

Crystalline structures of synthesized composites were verified through advanced X-ray diffraction (XRD) in a 2θ range of 10−80° with a scan rate of 0.01°/s. MDI JADE 6.5 software has been used for all refinements. The detailed surface morphology of the powders and the cross-sectional view of the fuel cell device were analyzed via field-emission scanning electron microscopy (FE-SEM) (JEOL JSM7100F Japan). The microstructure, interface confirmation, and elemental analysis and mapping were determined via high resolution-TEM (HR-TEM) (Tecnai G2 F30 S-TWIN 300 kV/FEG) reinforced by EDS (Oxford). The absorption spectra were recorded via UV−vis

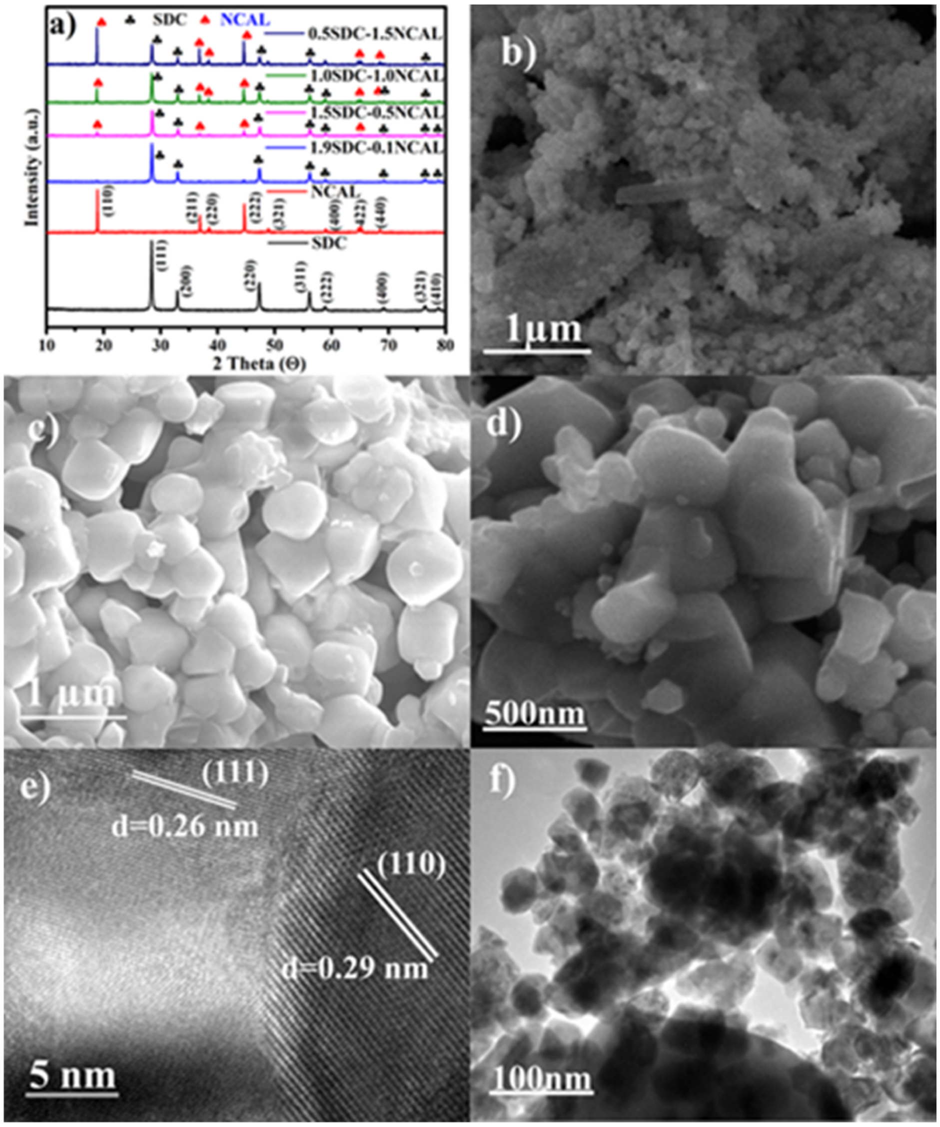

Figure 2. XRD pattern of various compositions of LNCA, SDC, and LNCA-SDC (0.1:1.9; 0.5:1.5; 1.0:1.0: 1.5:0.5) (a); FE-SEM images of LNCA, SDC, and (0.5LNCA:1.5SDC) (b−d); HR-TEM images displayed *d*-spacing and particles distribution of (0.5LNCA:1.5SDC) (e,f).

spectroscopy in the wavelength range of 300−800 nm to calculate the energy band gap. In addition, the valence band maxima were calculated via UPS, and the chemical oxidation states were determined by the X-ray photoelectron spectroscopy (XPS) using Al Kα radiation (1486.7 eV).

2.2. Fuel Cell Device Fabrication. It is known that there are three components of the fuel cell, such as electrolyte, anode, and cathode; therefore, there is a need to prepare each part of the fuel cell device. In this regard, to prepare electrodes, an appropriate volume of mixing medium, terpineol, was poured into the known amount of $LiNi_{0.8}Co_{0.15}Al_{0.05}O_2$ (LNCA) powder to prepare the slurry. Afterward, the prepared slurry was coated over the surface of the Ni-foam and then dried for 0.5 h at 150 °C in an open air oven to prepare the Ni-LNCA. Furthermore, the prepared LNCA-SDC powder was dry-pressed in between the two electrodes Ni-LNCA under the applied pressure of 220−250 MPa to prepare the cell with the structure of Ni-LNCA/0.5 LNCA-1.5 SDC/LNCA-Ni. The cell involving the diameter, thickness, and surface active area were approximately calculated as 13 mm, 1.5 mm, and 0.64 cm^2, respectively. Afterward, as the current collector, silver paste was applied on the both surfaces of the cell, and then, the prepared fuel cell device was heat-treated for 1 h at 600 °C prior to the electrochemical characterizations. Similarly, the pellets of other compositions and SDC were prepared under the same conditions for fuel cell applications. Moreover, the bi-layer of Ni-LNCA/LNCA-SDC was prepared for the confirmation of junction formation via the $I-V$ rectification phenomenon.

2.3. Electrochemical Performances. The fuel cell performance of the cell in terms of current−voltage and current power densities ($I-V-P$) was measured for the designed fuel cell device at 520−420 °C, supplying the H_2/air as a fuel and oxidant at the supply rate of 130 mL min^{-1}. The electrochemical performance of the fuel cell device was measured by employing the IT8511 electronic load (ITECH8511, ITECH Electrical Co., Ltd), where the IT7000 software was utilized to record the data at a scan rate of 0.02 A/s. Moreover, the Gamry Reference 3000 electrochemical workstation (Gamry Instruments, USA) was employed to investigate and record the electrochemical impedance spectra (EIS) under open-circuit voltage (OCV) mode in the frequency range of 0.1−10^5 Hz. The EIS raw data were extracted via the ZSimpWin software, and the raw data were fitted via the designed circuit for further interpretation.

3. RESULTS AND DISCUSSION

3.1. Structural and Morphological Analysis. The crystalline structure and phase of various LNCA-SDC composites were studied and are shown in Figure 2a. The depicted peaks of each component of the composite are (110),

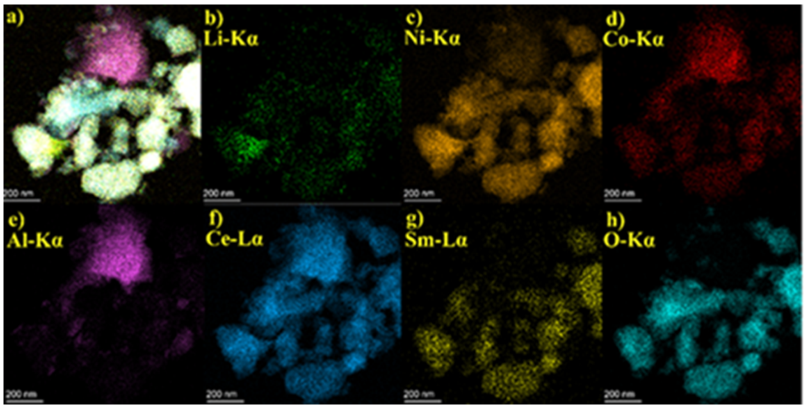

Figure 3. Mixed color HAAD-field image at 100 nm assisted via TEM (a); the corresponding EDS mapping elements involved in the 0.5LNCA:1.5SDC composite (b−h).

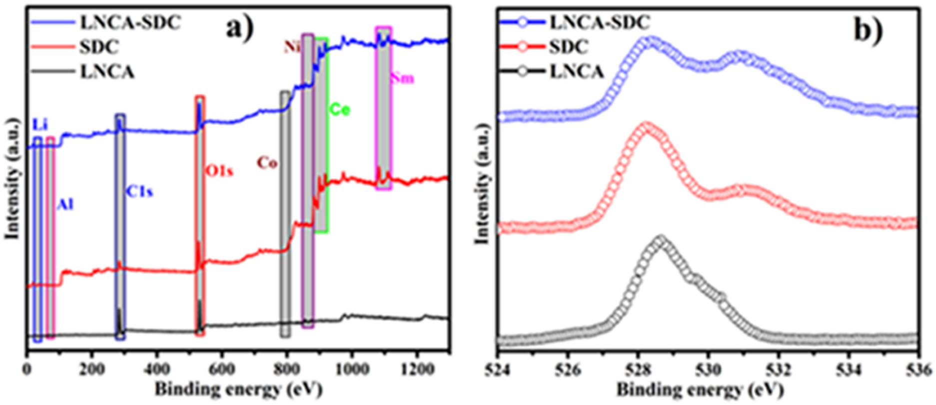

Figure 4. XPS analysis involving the complete survey (a); O 1s spectra (b) of LNCA, SDC, and 0.5 LNCA:1.5 SDC heterostructure composites.

(211), (220), (222), (321), (400), (422), and (440) corresponding to LNCA, and the diffraction peaks (111), (200), (220), (311), (222), (400), (321), and (410) are associated to SDC. It shows that each composition has peaks related to LNCA and SDC having a two-phase structure and good crystallinity according to their components. There is no additional peak observed, which ruled out the possibility of impurity or secondary peak formation. Scherer's formula was employed to calculate the average crystalline size, $D = k\lambda/\beta \cos \theta$; where the parameters D, k, λ, and β are crystalline size, constant ($k = 0.94$), wavelength, and full width at half maximum (fwhm), respectively. The average crystallite size of the LNCA-SDC composite from XRD spectra is in between 50 and 42 nm. In addition, there is a slight shift in the peak position of XRD spectra that represents the change in the lattice parameters or mismatch of ionic radii of Ni^{+2}, Al^{+3}, Li^{-1}, and Co^{+2} ions. In addition, the phase transformation and the reduction of LNCA (as an anode) was studied and presented by the XRD patterns of the on-line hydrogen-treated LNCA for 4 h in contrast to pure (raw) LNCA, as depicted in Figure S1. It can be seen that after the on-line treatment of LNCA in a H_2 environment, the strong metal Ni peaks appear and the number of NiO peaks was also identified as well the few main diffraction peaks also exist. The formation of NiO peaks is probably due to the cooling process, where the re-oxidation of Ni occurred. Besides, the surface morphology of LNCA, SDC, and 0.5LNCA:1.5SDC was studied via FE-SEM, as depicted in Figure 2b−d. It can be seen that particles of individual components are not highly homogenous with irregular morphology. In addition, the formation of the composite leads to the particle's homogenous distribution, good interconnection, and close contact with each other as compared to individual components. The higher compactness among particles and their nano-size distribution with less pores in the morphology assist the electrochemical process.[37,38] Moreover, the H_2-treated LNCA was further studied employing SEM analysis; therefore, the corresponding images and the enlarged view of both pure (raw powder) and H_2-treated LNCA are presented in Figure S2a,b. According to the corresponding images, the surface morphology of treated LNCA is considerably changed in contrast to the pure LNCA, as the surface turned rough as compared to the pure raw LNCA. Further, it can be seen that there are several small particles that appeared at the surface of treated LNCA, as shown in the enlarged image of Figure S2b, and this can lead to the formation of the Ni metal due to the H_2 treatment.[39,40] It was also evident by the XRD analysis that there are formations of Ni metals after treatment of raw LNCA in a H_2 environment.

Moreover, the high-resolution TEM was employed to study microstructures and investigate the interface formation, where the TEM images clearly display that the composite involving two different phases are distributed homogenously and form a percolated network. Further, the LNCA-SDC composite shows the wide interface formation, which assists in the fast ion transport acted upon the electrolyte, as depicted in Figure 2e,f. The lattice fringes and their calculated d-spacing values of LNCA and SDC with facets of (110) and (111) planes were

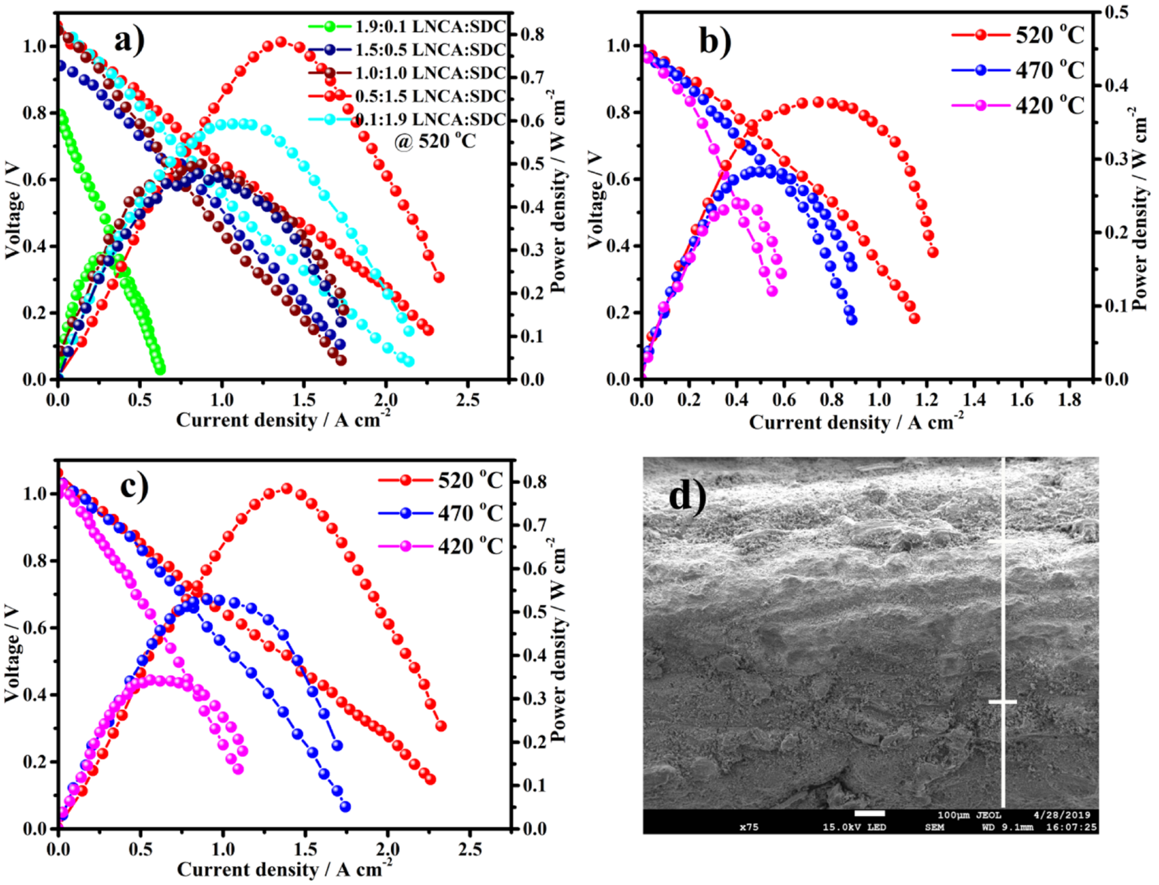

Figure 5. Electrochemical performance of the fuel cell device of various compositions of LNCA-SDC [(1.9:0.1), (1.5:0.5), (1.0:1.0), (0.5:1.5), and (0.1:1.9)] (a); ionic conductor SDC (b); semiconductor-ionic composite LNCA-SDC (0.5:1.5) at 520−420 °C (c); and fuel cell device SEM cross-sectional view of the Ni-LNCA/LNCA-SDC/LNCA-Ni (d).

0.29 and 0.26 nm, respectively (Figure 2e). The formation of a high conductance interface provides a steeper pathway for ionic transport in the case of using the LNCA-SDC as an electrolyte in the electrochemical operation. Moreover, the distribution of particles is depicted in Figure 2f, which is analogous to the SEM image (Figure 2d). Furthermore, there are many interfaces formed among the particles/grains shown in the TEM image (Figure 2f), where the large number of interfaces and homogenous distribution support the electrochemical reaction.

Moreover, the targeted composition and the elemental mapping of each component were investigated accurately via EDS assisted by TEM. The high angle annular dark (HAAD) image with their mixed colors of the particles of the prepared LNCA-SDC composite are presented in Figure 3a. Furthermore, the EDS mapping enables us to show the right and accurate composition mapping distinction of each element according to their contribution in 0.5LNCA-1.5SDC composite, as shown in Figure 3b−h.

3.2. XPS Analysis. The XPS spectra reveal the survey of each individual element in their respective components of LNCA and SDC as well in the heterostructure of LNCA-SDC, as represented in Figure 4a. Apparently, it can be clearly observed that there is a peak shift in O 1s spectra due to construction of LNCA-SDC. It can be observed that there is peak shifting and peak broadening in the O 1s spectra of the LNCA-SDC heterostructure composite, and the peak shifting and broadening toward higher binding energy illustrate the formation of higher oxygen vacancies at the interface of heterostructure composite, as presented in Figure 4b. It can be seen that there is an increase of peak intensity of oxidant oxygen at 530.4 eV; a broad and high intensity of the peak formed near 531.2 eV corresponds to O−H bonds as a result of hydration, as displayed in Figure 4b. Therefore, the analysis of the XPS infers that the higher oxygen vacancy formation leads to the fast and high transport of ion conduction during the electrochemical process.

3.3. Electrochemical Fuel Cell Performance. The electrochemical fuel cell performances of SDC and LNCA-SDC electrolytes in the fuel cells are presented as (I−V−P) characteristics of the fuel cell devices measured with the structure of Ni-LNCA/SDC/LNCA-Ni and Ni-LNCA/LNCA-SDC/Ni-LNCA at 520−420 °C. Initially, various compositions of LNCA-SDC are evaluated at 520 °C to assess the best optimal weight ratio of composites, where the best power output and high OCV of the composite can be observed in Figure 5a. Figure 5b displays the fuel cell performance of the pure ionic conductor SDC electrolyte at 520−420 °C. However, the appropriate optimal weight ratio of LNCA-SDC (0.5:1.5) showed the high OCV (1.04 V) and yielded remarkable power output of 0.735 W cm^{-2} at 520 °C, as respectively presented in Figure 5c. It should be reported that a high value of OCV revealed that there is no current leakage in the device; and the high-power density and sufficient OCV of LNCA-SDC confirmed that the design and principle of

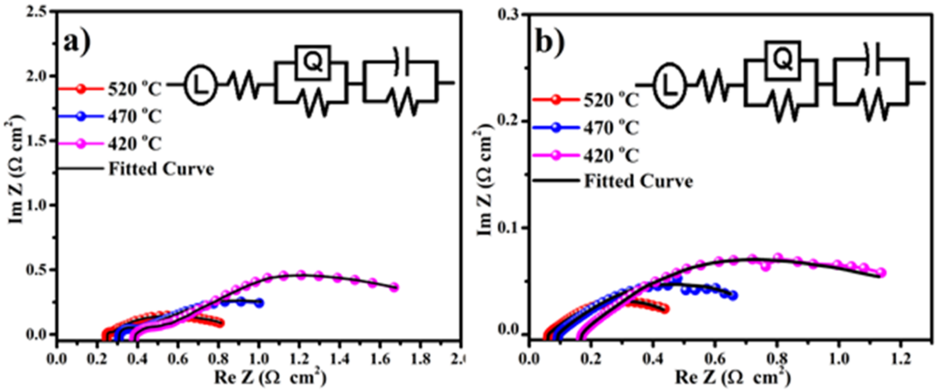

Figure 6. Electrochemical impedance spectroscopy of the SDC and LNCA/SDC (0.5:1.5) in the temperature range of 520−420 °C (a,b).

Table 1. Extracted EIS Fitted Data of SDC at Temperature 520−420 °C, Where [R−Ω cm^2], {Q−Y_o[(s−s)^n cm^{-2}]}, and [C−F cm^{-2}] and n is 0 < n < 1, Q is in Henry

composition	L	R_o	R_1	Q (CPE)	C	R_2	n
				SDC			
520 °C	1.08×10^{-8}	0.21	0.09	0.452	5.245×10^{-5}	0.59	0.432
470 °C	1.20×10^{-7}	0.31	0.12	0.211	7.452×10^{-3}	0.72	0.541
420 °C	7.12×10^{-8}	0.39	0.18	0.071	2.245×10^{-2}	1.12	0.324

Table 2. Extracted EIS Fitted Data of 0.5 LNCA:1.5 SDC at Temperature 520−420 °C, Where [R−Ω cm^2], {Q−Y_o[(s−s)^n cm^{-2}]}, and [C−F cm^{-2}] and n is 0 < n < 1, Q is in Henry

composition	L	R_o	R_1	Q (CPE)	C	R_2	n
				LNCA-SDC			
520 °C	1.02×10^{-7}	0.05	0.39	2.811	4.845×10^{-7}	0.05	0.452
470 °C	1.53×10^{-7}	0.09	0.59	0.972	5.784×10^{-6}	0.1	0.512
420 °C	2.76×10^{-7}	0.16	0.78	0.541	2.784×10^{-6}	0.18	0.811

semiconductor-ionic electrolyte membrane fuel cells are reliable.

On the other hand, the compositions utilized in fuel cell devices, where LNCA is dominant as compared to SDC, showed lower OCV (<1.0 V) due to the particular reason that p-type semiconductor LNCA has high electron (hole) charge species, which decreased the OCV and lowered the power output. The other possible reason could be the porous morphology of LNCA, which allows for gas leakage and portrays low OCV. Furthermore, it has been reported that SDC is a pure ionic conductor,[41] where the introduction of SDC into LNCA to construct the LNCA-SDC composite enhances power density significantly as well increases the OCV, respectively. Indeed, the formation of the interface in the semiconductor-ionic heterostructure composite materials significantly assists in the enhancement of ionic conductivity significantly.[25,42] However, there is also a question raised: how can the semiconductor-ionic composite gain such enhanced ionic conductivity? We already know that the presence of electronic conductivity has a negative impact in the fuel cell device but has also the positive impact. It can be explained in such a way that the sufficient electronic conduction in the composite assisted in extending the triple-phase boundary (TPB) area at both electrodes functional regions, which helps in reducing the electrode polarization.[43] Therefore, the TPB support the electrochemical process and assist in the enhancement of charge and mass transfer to obtain high fuel cell performance. In addition, the present optimized composite of LNCA-SDC maintained primary part of SDC, which contribute the ionic conduction. Besides, the composites with dominant LNCA maintaining higher electronic (holes) conductivity with weight ratios of LNCA-SDC (1.5:0.5 and 1.9:0.1) displayed lower OCV (<1.0 V) and electrochemical fuel cell performance, respectively.

Moreover, the cross-sectional view extracted by SEM of the fuel cell device, where a clear interface can be observed among electrolytes and electrodes, as depicted in Figure 5d. Moreover, the device shows no cracks, which reveal the tightness to avoid any gas leakage. Furthermore, the optimal weight ratio of LNCA-SDC (0.5:1.5) was employed for further electrochemical characterizations. Likewise, the electrical properties of SDC and LNCA-SDC composites have been investigated through EIS.

3.4. Electrochemical Impedance Spectroscopy. The charge transport and their barriers are studied through EIS analysis of SDC and LNCA-SDC heterostructure composite as electrolytes in the fuel cell in frequency range of 0.1−10^5 Hz under OCV conditions at 520−420 °C. The Nyquist plots of SDC and LNCA-SDC composites as electrolytes are presented in Figure 6. The power output of the fuel cell is directly correlated and evaluated in terms of the internal resistances, such as Ohmic and polarization resistances (R_o and R_p) that provide the information for the charge transport illustrated by the EIS measurements. The EIS raw data were fitted via the equivalent circuit of LR_o-QR_1-CR_2 using the ZSimpWin software, as shown in Figure 6, and the raw data are enlisted in Tables 1 and 2. Besides, the Ohmic resistance (R_o) corresponds to the intersection of the EIS curve at the high frequency on the real axis of resistance, which most often offered by the ionic transport resistance in the electrolyte layer. Further, the other two resistances (R_1 and R_2) is the sum of both resistances called polarization resistance (R_p) and relate to charge and mass transfer at the intermediate- and low-frequency arc process zones due to the electrochemical process of electrodes.

Besides, to investigate the electrical charge carriers quantitatively, the obtained R_o and R_p values for the typical ionic electrolyte SDC are higher than the R_o and R_p values of the LNCA-SDC composite, respectively, as shown in Tables 1 and 2. However, the reason behind this could be the coupling effect of the semiconductor and ionic conductor, where an additional oxygen vacancy content enrichment can be formed at the interface of LNCA-SDC, and the depletion of oxygen vacancies in the interface can be eliminated.[21,44] Consequently, there is an enhancement in the ionic conduction of the LNCA-SDC semiconductor-ionic composite. Conventionally, it is perceived that the electronic nature of materials used as an electrolyte causes short-circuiting. In contrast, in our case, the presence of electronic charge species helps in the formation of the built-in field. Interestingly, the presence of mixed ionic-electronic nature of the LNCA-SDC composite material provides room for fuel cell technology to replace the pure ionic membrane, which constrained the SOFC advancement in terms of operating at low temperature.

Moreover, the total conductivity is obtained from the extracted parameters of EIS via an equivalent circuit, where total conductivity includes ionic and electronic conduction. The following relation has been utilized to calculate the total conductivity, σ_t, $\sigma_t = L/RA$, where L, R, and A correspond to thickness, resistance, and total active area of the cell, respectively. Rather than EIS results, we calculated the ionic conductivity of SDC and LNCA-SDC via the known method reported previously using the slope of the $I-V$ curve (Figure 5b,c) at the Ohmic polarization region, as shown in Figure 7.[45,46] The attained ionic conductivity of SDC obtained from the $I-V$ polarization curve was 0.022 S cm^{-1} at 520 °C. However, the introduction of SDC into LNCA to construct the LNCA-SDC heterostructure has significantly increased the electrochemical performance due to the enhancement of ionic conduction. Therefore, the LNCA-SDC displayed the ionic conductivity of σ_i = 0.12 S cm^{-1} at 520 °C, as depicted in Figure 7. This enhancement of ionic conductivity in LNCA-SDC leads to a remarkable enhancement in electrochemical performance, which helps to establish a strong built-in electric field in the semiconductor-ionic heterostructure to assist in the fast ion migration. Moreover, there is also a possibility of protonic conduction introduced by LNCA because the layered structures have protonic conduction in the fuel cell condition. Hence, the presence of different kinds of conduction in the composite materials leads to the enhancement of electrochemical fuel cell performance.[18] Besides, the activation energy of the LNCA-SDC heterostructure composite was calculated, that is, 0.51 eV at 520 °C, where the low activation energy contributed to high ionic conductivity and electrochemical performance.

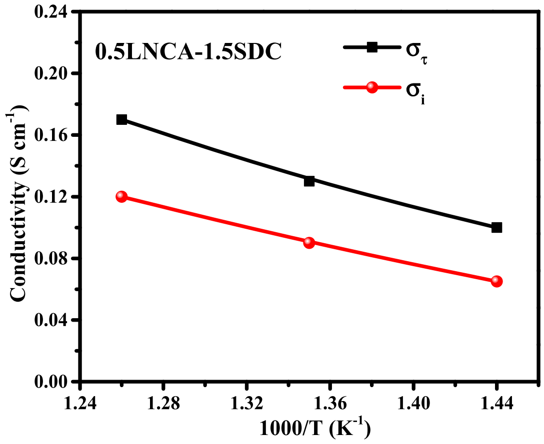

Figure 7. Total and ionic conductivities of the 0.5 LNCA-1.5 SDC heterostructure at various temperatures from 520 to 420 °C.

3.5. Optical Properties. The concept of employing semiconductors and their heterostructure with evidence of experimental results rolled out the conventional fuel cell concept that semiconductor oxide material-based electrolyte maintains electronic behavior, which can not be employed in fuel cell application. The abovementioned results clearly demonstrated that the introduction of semiconductors and formation of their heterostructure not only replaced the conventional fuel cell concept but also displayed the enhanced ionic conductivity with significant electrochemical performance at low operational temperature. Moreover, a detailed study of the formation of the heterojunction of a semiconductor-ionic LNCA-SDC heterostructure was analyzed by energy band structure tuning and UV analysis, and the relevant data can provide us confirmation of the semiconducting nature of the prepared samples. The energy band gaps are determined from the absorption spectra obtained from UV−vis spectroscopy, following the relation $\alpha h\nu = A(h\nu - E_g)^{1/2}$, where α, h, E_g, and A are the absorption coefficient, photon energy, optical band gap energy, and constant.[47] The energy band gap values can be estimated via drawing of the Tauc plot of $(\alpha h\nu)^2$ against photon energy ($h\nu$). The absorbance and energy band gaps of various composites are presented in Figure S3a,b. Furthermore, the obtained energy band gap of LNCA is 0.98 eV and the band gap of SDC is 2.9 eV is shown in Figure 8a,b. It is found when the LNCA content is higher than 0.5 in the weight ratio, then the fuel cell performance will decrease with the reduction of Eg.

3.6. Reconstruction of the Energy Band Structure and Working Principle. According to the principle of conventional FCs, the presence of electronic characteristics is not feasible for electrolyte application. Semiconductor heterostructure technology has proven to deliver not only higher conductivity but also better performance and higher OCV even at low operating temperatures in comparison with conventional fuel cell technology. The heterostructure of a semiconductor-ionic composite based on p−n heterojunction was constructed, as illustrated in Figure 9. The formation of a heterojunction can be confirmed from the energy band structure (i.e., UV and UPS). The band gap values obtained from absorbance of LNCA is 0.98 eV and SDC with 2.9 eV, respectively. Furthermore, the valence band maxima were obtained by employing the UPS. Thus, the valence band conduction value V_b value was calculated following the relation, $\varphi = 21.2 - (E_{\text{cuttoff}} - E_{\text{onset}})$, where $h\nu$ denotes incident He (I) energy, which is 21.2 eV, where E_{cuttoff} and E_{onset} are the higher and lower binding energy, respectively, displayed in energy offsets in UPS raw data, as shown in Figure 9a,b.[48] The V_b (valence band) values were obtained using the

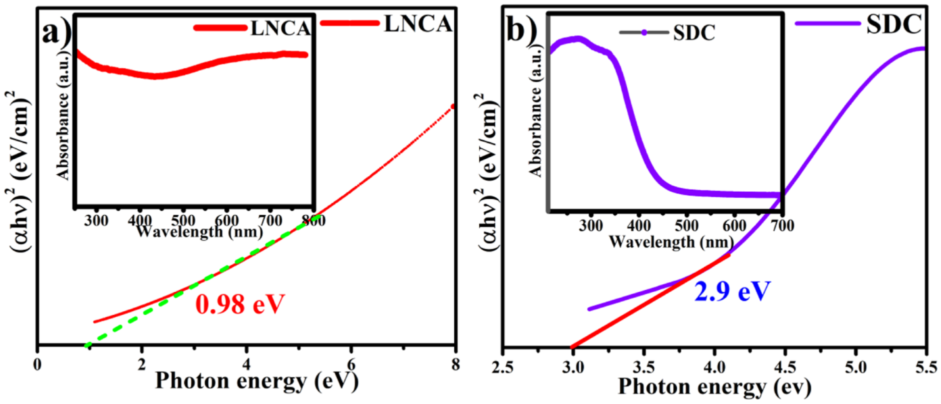

Figure 8. UV−vis spectroscopy absorbance and band gap calculation configuration of LNCA and SDC (a,b).

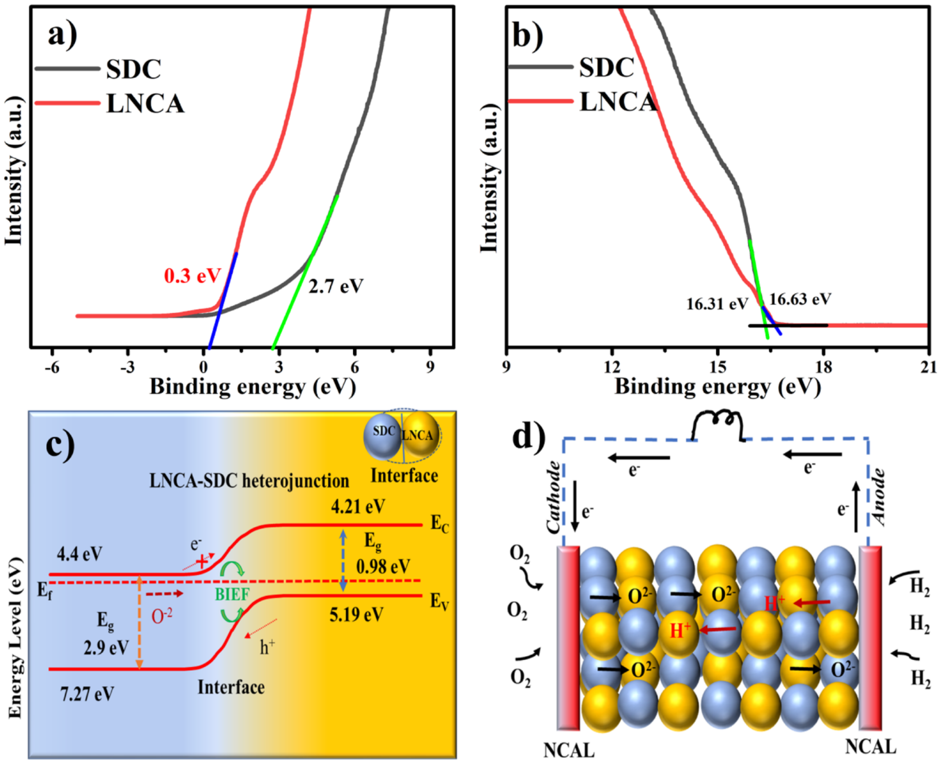

Figure 9. UPS analysis of LNCA and SDC (a,b); energy band structure diagram of LNCA and SDC (c); and fuel cell diagram mechanism (d).

UPS are 5.19 and 7.27 eV, respectively, where the conduction band (C_b) values were calculated using this relation ($E_g = C_b + V_b$). Further, C_b was obtained by adding the values V_b and E_g, where the calculated C_b values are 4.21 and 4.4 eV corresponding to the LNCA and SDC, as shown in Figure 9c. Employing the energy band gap and valence band maxima values in the formation of energy band structure, where the semiconductor and ionic conductor have different Fermi levels; thus, the combination of dissimilar particles/grains with different Fermi levels will reach to an equilibrium of same Fermi level at the interface leading to the band bending resulted in potential barrier at the interface region. Therefore, the induced potential barrier creates an electric field, which supports the transport of ions at the interface region and restricts the intrinsic electronic flow in semiconductor-ionic composite electrolytes.[22,49] Moreover, there is an involvement of intrinsic electrons (holes) that contribute to create the built-in field, which provides a fast route to the transport of ions.[50,51] Also, Figure 9d shows the schematic illustration and the working mechanism of fuel cell.

3.7. Junction Effect of the Heterostructure Composite.

The prepared LNCA-SDC heterostructure electrolyte material has been utilized to construct the asymmetric/bi-layer structure device such as Ni-LNCA/LNCA-SDC to analyze the electrons blocking at the interface of metallic Ni and electrolytes by the junction effect formation in the bi-layer device via a rectification phenomenon. Moreover, the detailed study was performed by the demonstration of the asymmetric device in different environments of air and H_2/air to observe the Schottky Junction (SJ) to recognize the rectification phenomenon at 520 °C. Initially, the asymmetric device was studied in the air environment in the biased voltage range of −1.5−1.5 V at 520 °C, where the corresponding *I*−*V* curve data were recorded, as shown in Figure 10a. The *I*−*V* characteristics curve clearly indicates that it followed the Ohm's law and can be presented by the following relation *I* =

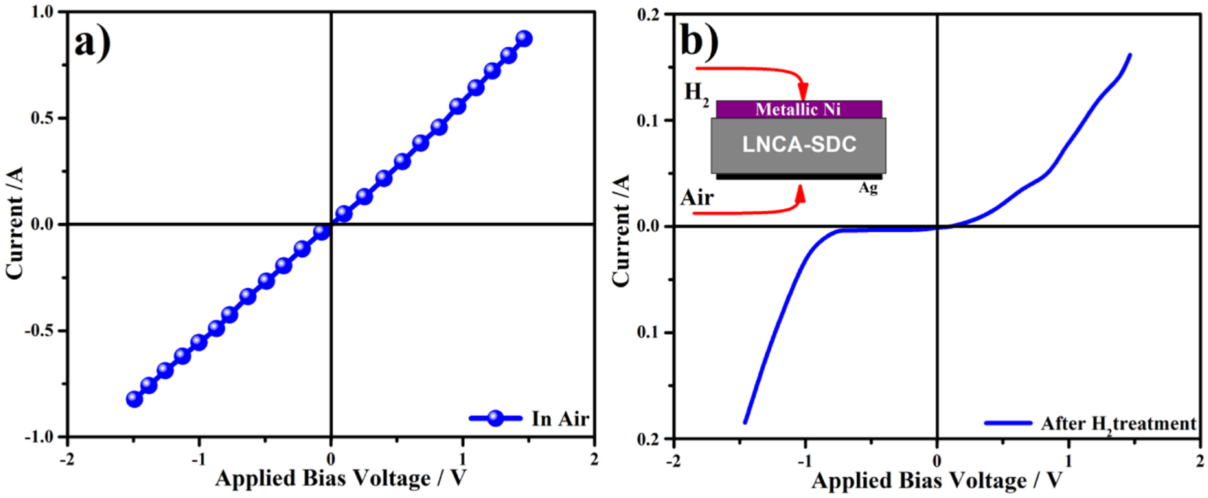

Figure 10. $I-V$ characteristics curve analysis of the 0.5 LNCA:1.5 SDC heterostructure under the bias voltage in various environments (a,b).

V/R. Thus, the formation of the $I-V$ characteristics curve following Ohm's law suggests no junction formation, as shown in Figure 10a. Furthermore, the same bi-layer device was studied in different environments of H_2/air; therefore, initially, H_2 was supplied for 0.5 h and tends to reduce, and later, the corresponding $I-V$ data were obtained through recording the produced current under the bias voltage of −1.5 to 1.5 V and are presented in Figure 10b. It can be seen that the increase of bias voltage (in Figure 10b) tends to reduce resistance and increase current simultaneously. Consequently, there is an improvement in diode behavior, which ensued with the passage of time and suggested the formation of SJ from the direction of the metallic Ni leads toward the semiconductor electrolyte layer LNCA-SDC; it also assists in the formation of a built-in field. The formation of SJ and built-in electric field assist in blockage of electronic flow as well as support the fast ion (O^{2-}/H^+) conduction.[27,52−54]

4. CONCLUSIONS

The present work provides new insights into the improvement of ionic conduction and electrochemical performance based on semiconductor-ionic heterostructure composite membranes. Various compositions of LNCA-SDC were studied, where the weight ratio of 0.5 LNCA-1.5 SDC demonstrated remarkable results. The optimized composite of the LNCA-SDC heterostructure delivered an excellent power output of 0.735 W cm^{-2} at 520 °C. Interestingly, the introduction of an ionic conductor into semiconductors significantly enhanced the ionic conductivity in the heterostructure electrolyte, which is desirable to achieve a high electrochemical performance. The energy band engineering leads to the high and fast passage of ion conduction at the interface region of the LNCA-SDC heterostructure. Moreover, the interface played a vital role in fast transport of ion conduction, and the formation of the built-in electric field assisted in the fast and high transport of ion conduction at the interface. Moreover, XPS analysis also revealed that there is a formation of high content of oxygen vacancies at the interface to support the high conduction of ion conduction. In addition, the junction formation was verified in between metallic Ni and LNCA-SDC, which assisted in the suppression of electronic conduction to avoid short-circuiting problems. All these characteristics offer innovative insights to design unique electrolytes based on this concept.

■ ASSOCIATED CONTENT

Supporting Information

The Supporting Information is available free of charge at https://pubs.acs.org/doi/10.1021/acsaem.1c01186.

XRD patterns of LNCA raw powder and the LNCA as an anode, surface morphology of the LNCA raw powder and the LNCA as an anode, and UV-Vis spectroscopy absorbance and energy band gaps calculation configuration of various compositions of LNCA-SDC (PDF)

■ AUTHOR INFORMATION

Corresponding Authors

Changping Yang − *Hubei Collaborative Innovation Center for Advanced Organic Chemical Materials, Faculty of Physics and Electronic Science, Hubei University, Wuhan, Hubei 430062, China; Faculty of Materials Science and Engineering, Taiyuan University of Science and Technology, Taiyuan 030024, China*; Email: cpyang@hubu.edu.cn

Shi Heng Liang − *Hubei Collaborative Innovation Center for Advanced Organic Chemical Materials, Faculty of Physics and Electronic Science, Hubei University, Wuhan, Hubei 430062, China*; Email: shihengliang@hubu.edu.cn

Muhammad Imran Asghar − *Hubei Collaborative Innovation Center for Advanced Organic Chemical Materials, Faculty of Physics and Electronic Science, Hubei University, Wuhan, Hubei 430062, China; New Energy Technologies Group, Department of Applied Physics, Aalto University School of Science, FI-00076 Aalto Espoo, Finland*; orcid.org/0000-0003-3559-0955; Email: imran.asghar@aalto.fi

Authors

Zuhra Tayyab − *Hubei Collaborative Innovation Center for Advanced Organic Chemical Materials, Faculty of Physics and Electronic Science, Hubei University, Wuhan, Hubei 430062, China*

Sajid Rauf − *Hubei Collaborative Innovation Center for Advanced Organic Chemical Materials, Faculty of Physics and Electronic Science, Hubei University, Wuhan, Hubei 430062, China; College of Electronics and Information Engineering, Shenzhen University, Shenzhen, Guangdong Province 518000, China*

Chen Xia − *Hubei Collaborative Innovation Center for Advanced Organic Chemical Materials, Faculty of Physics* *and Electronic Science, Hubei University, Wuhan, Hubei 430062, China;* orcid.org/0000-0002-3133-7031

Baoyuan Wang − *Hubei Collaborative Innovation Center for Advanced Organic Chemical Materials, Faculty of Physics and Electronic Science, Hubei University, Wuhan, Hubei 430062, China;* orcid.org/0000-0002-8857-3318

M.A.K. Yousaf Shah − *Jiangsu Provincial Key Laboratory of Solar Energy Science and Technology/Energy Storage Joint Research Center, School of Energy and Environment, Southeast University, Nanjing 210096, China;* orcid.org/0000-0002-1081-9090

Naveed Mushtaq − *Jiangsu Provincial Key Laboratory of Solar Energy Science and Technology/Energy Storage Joint Research Center, School of Energy and Environment, Southeast University, Nanjing 210096, China*

Peter D. Lund − *New Energy Technologies Group, Department of Applied Physics, Aalto University School of Science, FI-00076 Aalto Espoo, Finland;* orcid.org/0000-0002-4819-3847

Complete contact information is available at: https://pubs.acs.org/10.1021/acsaem.1c01186

Funding

This study was supported by National Natural Science Foundation of China (NSFC) under grant no. 11674086, 11904088, and 2019CFB183. Scientific Research Project of Education Department of Hubei Province (no. Q20191010) and Research Project of Wuhan Science and Technology Bureau (no. 2019010701011394). Dr. Asghar thanks the Hubei Talent 100 program and Academy of Finland (Grant nos. 13329016, 13322738) for their support.

Notes

The authors declare no competing financial interest.

■ REFERENCES

(1) Fan, L.; Zhu, B.; Su, P.-C.; He, C. Nanomaterials and technologies for low temperature solid oxide fuel cells: recent advances, challenges and opportunities. *Nano Energy* **2018**, *45*, 148−176.

(2) Wachsman, E. D.; Lee, K. T. Lowering the temperature of solid oxide fuel cells. *Science* **2011**, *334*, 935−939.

(3) Skinner, S. J.; Kilner, J. A. Oxygen ion conductors. *Mater. Today* **2003**, *6*, 30−37.

(4) Ormerod, R. M. Solid oxide fuel cells. *Chem. Soc. Rev.* **2003**, *32*, 17−28.

(5) Rivera, A.; Santamaría, J.; León, C. Electrical conductivity relaxation in thin-film yttria-stabilized zirconia. *Appl. Phys. Lett.* **2001**, *78*, 610−612.

(6) Chen, Y.-Y.; Wei, W.-C. J. Processing and characterization of ultra-thin yttria-stabilized zirconia (YSZ) electrolytic films for SOFC. *Solid State Ionics* **2006**, *177*, 351−357.

(7) Huang, H.; Nakamura, M.; Su, P.; Fasching, R.; Saito, Y.; Prinz, F. B. High-performance ultrathin solid oxide fuel cells for low-temperature operation. *J. Electrochem. Soc.* **2006**, *154*, B20.

(8) Shim, J. H.; Chao, C.-C.; Huang, H.; Prinz, F. B. Atomic layer deposition of yttria-stabilized zirconia for solid oxide fuel cells. *Chem. Mater.* **2007**, *19*, 3850−3854.

(9) Kerman, K.; Lai, B.-K.; Ramanathan, S. Nanoscale compositionally graded thin-film electrolyte membranes for low-temperature solid oxide fuel cells. *Adv. Energy Mater.* **2012**, *2*, 656−661.

(10) Takagi, Y.; Lai, B.-K.; Kerman, K.; Ramanathan, S. Low temperature thin film solid oxide fuel cells with nanoporous ruthenium anodes for direct methane operation. *Energy Environ. Sci.* **2011**, *4*, 3473−3478.

(11) Tsuchiya, M.; Lai, B.-K.; Ramanathan, S. Scalable nanostructured membranes for solid-oxide fuel cells. *Nat. Nanotechnol.* **2011**, *6*, 282−286.

(12) Su, P.-C.; Chao, C.-C.; Shim, J. H.; Fasching, R.; Prinz, F. B. Solid oxide fuel cell with corrugated thin film electrolyte. *Nano Lett.* **2008**, *8*, 2289−2292.

(13) Rauf, S.; Zhu, B.; Shah, M. A. K. Y.; Xia, C.; Tayyab, Z.; Ali, N.; Yang, C.; Mushtaq, N.; Asghar, M. I.; Akram, F.; Lund, P. D. Tailoring triple charge conduction in $BaCo_{0.2}Fe_{0.1}Ce_{0.2}Tm_{0.1}Zr_{0.3}Y_{0.1}O_{3-\delta}$ semiconductor electrolyte for boosting solid oxide fuel cell performance. *Renewable Energy* **2021**, *172*, 336−349.

(14) Chen, G.; Zhu, B.; Deng, H.; Luo, Y.; Sun, W.; Liu, H.; Zhang, W.; Wang, X.; Qian, Y.; Hu, X.; Geng, S.; Kim, J.-S. Advanced Fuel Cell Based on Perovskite La−$SrTiO_3$ Semiconductor as the Electrolyte with Superoxide-Ion Conduction. *ACS Appl. Mater. Interfaces* **2018**, *10*, 33179−33186.

(15) Rauf, S.; Zhu, B.; Shah, M. Y.; Tayyab, Z.; Attique, S.; Ali, N.; Mushtaq, N.; Asghar, M. I.; Lund, P. D.; Yang, C. P. Low-temperature solid oxide fuel cell based on Tm-doped $SrCeO_{2-\delta}$ semiconductor electrolyte. *Mater. Today Energy* **2021**, *20*, 100661.

(16) Lan, R.; Tao, S. Novel proton conductors in the layered oxide material $Li_xlAl_{0.5}Co_{0.5}O_2$. *Adv. Energy Mater.* **2014**, *4*, 1301683.

(17) Zhou, Y.; Guan, X.; Zhou, H.; Ramadoss, K.; Adam, S.; Liu, H.; Lee, S.; Shi, J.; Tsuchiya, M.; Fong, D. D.; Ramanathan, S. Strongly correlated perovskite fuel cells. *Nature* **2016**, *534*, 231−234.

(18) Rauf, S.; Shah, M. A. K. Y.; Zhu, B.; Tayyab, Z.; Ali, N.; Attique, S.; Xia, C.; Khatoon, R.; Yang, C.; Asghar, M. I.; Lund, P. D. Electrochemical Properties of a Dual-Ion Semiconductor-Ionic $Co_{0.2}Zn_{0.8}O$-$Sm_{0.20}Ce_{0.80}O_{2-\delta}$ Composite for a High-Performance Low-Temperature Solid Oxide Fuel Cell. *ACS Appl. Energy Mater.* **2021**, *4*, 194−207.

(19) Rauf, S.; Zhu, B.; Shah, M. A. K. Y.; Tayyab, Z.; Attique, S.; Ali, N.; Mushtaq, N.; Wang, B.; Yang, C.; Asghar, M. I.; Lund, P. D. Application of a triple-conducting heterostructure electrolyte of $Ba_{0.5}Sr_{0.5}Co_{0.1}Fe_{0.7}Zr_{0.1}Y_{0.1}O_{3-\delta}$ and $Ca_{0.04}Ce_{0.80}Sm_{0.16}O_{2-\delta}$ for high performance low-temperature solid oxide fuel cell. *ACS Appl. Mater. Interfaces* **2020**, *12*, 35071−35080.

(20) Zhang, W.; Cai, Y.; Wang, B.; Deng, H.; Feng, C.; Dong, W.; Li, J.; Zhu, B. The fuel cells studies from ionic electrolyte $Ce_{0.8}Sm_{0.05}Ca_{0.15}O_{2-\delta}$ to the mixture layers with semiconductor $Ni_{0.8}Co_{0.15}Al_{0.05}LiO_{2-\delta}$. *Int. J. Hydrogen Energy* **2016**, *41*, 18761−18768.

(21) Wang, B.; Wang, Y.; Fan, L.; Cai, Y.; Xia, C.; Liu, Y.; Raza, R.; van Aken, P. A.; Wang, H.; zhu, B. Preparation and characterization of Sm and Ca co-doped ceria−$La_{0.6}Sr_{0.4}Co_{0.2}Fe_{0.8}O_{3-\delta}$ semiconductor−ionic composites for electrolyte-layer-free fuel cells. *J. Mater. Chem. A* **2016**, *4*, 15426−15436.

(22) Mushtaq, N.; Xia, C.; Dong, W.; Wang, B.; Raza, R.; Ali, A.; Afzal, M.; Zhu, B. Tuning the Energy Band Structure at Interfaces of the $SrFe_{0.75}Ti_{0.25}O_{3-\delta}$−$Sm_{0.25}Ce_{0.75}O_{2-\delta}$ Heterostructure for Fast Ionic Transport. *ACS Appl. Mater. Interfaces* **2019**, *11*, 38737−38745.

(23) Zhang, W.; Cai, Y.; Wang, B.; Xia, C.; Dong, W.; Li, J.; Zhu, B. Mixed ionic-electronic conductor membrane based fuel cells by incorporating semiconductor $Ni_{0.8}Co_{0.15}Al_{0.05}LiO_{2-\delta}$ into the $Ce_{0.8}Sm_{0.2}O_{2-\delta}$-$Na_2CO_3$ electrolyte. *Int. J. Hydrogen Energy* **2016**, *41*, 15346−15353.

(24) Yang, S. M.; Lee, S.; Jian, J.; Zhang, W.; Lu, P.; Jia, Q.; Wang, H.; Noh, T. W.; Kalinin, S. V.; MacManus-Driscoll, J. L. Strongly enhanced oxygen ion transport through samarium-doped CeO_2 nanopillars in nanocomposite films. *Nat. Commun.* **2015**, *6*, 1−8.

(25) Lee, S.; MacManus-Driscoll, J. L. Research Update: Fast and tunable nanoionics in vertically aligned nanostructured films. *APL Mater.* **2017**, *5*, 042304.

(26) Chiabrera, F.; Garbayo, I.; Tarancón, A. Nanoionics and interfaces for energy and information technologies. *Met. Oxide-Based Thin Film Struct.* **2018**, 409−439.

(27) Zhu, B.; Lund, P. D.; Raza, R.; Ma, Y.; Fan, L.; Afzal, M.; Patakangas, J.; He, Y.; Zhao, Y.; Tan, W.; Huang, Q.-A.; Zhang, J.;

Wang, H. Schottky junction effect on high performance fuel cells based on nanocomposite materials. *Adv. Energy Mater.* **2015**, *5*, 1401895.

(28) Fan, L.; Ma, Y.; Wang, X.; Singh, M.; Zhu, B. Understanding the electrochemical mechanism of the core−shell ceria−LiZnO nanocomposite in a low temperature solid oxide fuel cell. *J. Mater. Chem. A* **2014**, *2*, 5399−5407.

(29) Zhu, B.; Lund, P.; Raza, R.; Patakangas, J.; Huang, Q.-A.; Fan, L.; Singh, M. A new energy conversion technology based on nano-redox and nano-device processes. *Nano Energy* **2013**, *2*, 1179−1185.

(30) Zhang, H.; May, B. M.; Omenya, F.; Whittingham, M. S.; Cabana, J.; Zhou, G. Layered oxide cathodes for Li-ion batteries: oxygen loss and vacancy evolution. *Chem. Mater.* **2019**, *31*, 7790−7798.

(31) Chen, G.; Sun, W.; Luo, Y.; Liu, H.; Geng, S.; Yu, K.; Liu, G. Investigation of layered $Ni_{0.8}Co_{0.15}Al_{0.05}LiO_2$ in electrode for low-temperature solid oxide fuel cells. *Int. J. Hydrogen Energy* **2018**, *43*, 417−425.

(32) Yang, D.; Chen, G.; Liu, H.; Zhang, L.; He, Y.; Zhang, X.; Yu, K.; Geng, S.; Li, Y. Electrochemical performance of a $Ni_{0.8}Co_{0.15}Al_{0.05}LiO_2$ cathode for a low temperature solid oxide fuel cell. *Int. J. Hydrogen Energy* **2021**, *46*, 10438−10447.

(33) Fan, L.; Su, P.-C. Layer-structured LiNi0. 8Co0. 2O2: A new triple (H^+/O^{2-}/e^-) conducting cathode for low temperature proton conducting solid oxide fuel cells. *J. Power Sources* **2016**, *306*, 369−377.

(34) Yang, F.; Lu, Y.; Li, J.; Song, X.; Yu, L.; Cai, Y. Stability considerations of semiconductor ionic fuel cells from a LNCA ($LiNi_{0.8}Co_{0.15}Al_{0.05}O_{2-\delta}$) and Sm-doped ceria (SDC; $Ce_{0.8}Sm_{0.2}O_{2-\delta}$) composite electrolyte. *Int. J. Hydrogen Energy* **2021**, *46*, 9882−9888.

(35) Liu, X.; Dong, W.; Xia, C.; Huang, Q.; Cai, Y.; Wei, L.; Wu, G.; Wang, X.; Tong, Y.; Qiao, Z.; Meng, Y.; Mushtaq, N.; Wang, B.; Wang, H. Study on charge transportation in the layer-structured oxide composite of SOFCs. *Int. J. Hydrogen Energy* **2018**, *43*, 12773−12781.

(36) Zhang, Y.; Liu, J.; Singh, M.; Hu, E.; Jiang, Z.; Raza, R.; Wang, F.; Wang, J.; Yang, F.; Zhu, B. Superionic Conductivity in Ceria-Based Heterostructure Composites for Low-Temperature Solid Oxide Fuel Cells. *Nano-Micro Lett.* **2020**, *12*, 1−20.

(37) Shah, M. A. K. Y.; Rauf, S.; Mushtaq, N.; Tayyab, Z.; Ali, N.; Yousaf, M.; Xing, Y.; Akbar, M.; Lund, P. D.; Yang, C. P.; Zhu, B.; Asghar, M. I. Semiconductor Fe-doped $SrTiO_{3-\delta}$ perovskite electrolyte for low-temperature solid oxide fuel cell (LT-SOFC) operating below 520° C. *Int. J. Hydrogen Energy* **2020**, *45*, 14470−14479.

(38) Abdala, P. M.; Custo, G. S.; Lamas, D. G. Enhanced ionic transport in fine-grained scandia-stabilized zirconia ceramics. *J. Power Sources* **2010**, *195*, 3402−3406.

(39) Liu, X.; Dong, W.; Tong, Y.; Wei, L.; Yuan, M.; Wang, X.; Wang, B.; Zhu, B. Li effects on layer-structured oxide $Lix-Ni_{0.8}Co_{0.15}Al_{0.05}O_{2-\delta}$: improving cell performance via on-line reaction. *Electrochim. Acta* **2019**, *295*, 325−332.

(40) Wang, B.; Cai, Y.; Xia, C.; Kim, J.-S.; Liu, Y.; Dong, W.; Wang, H.; Afzal, M.; Li, J.; Raza, R.; Zhu, B. Semiconductor-ionic membrane of LaSrCoFe-oxide-doped ceria solid oxide fuel cells. *Electrochim. Acta* **2017**, *248*, 496−504.

(41) Liu, M.; Ding, D.; Bai, Y.; He, T.; Liu, M. An efficient SOFC based on samaria-doped ceria (SDC) electrolyte. *J. Electrochem. Soc.* **2012**, *159*, B661−B665.

(42) Cai, Y.; Chen, Y.; Akbar, M.; Jin, B.; Tu, Z.; Mushtaq, N.; Wang, B.; Qu, X.; Xia, C.; Huang, Y. A Bulk-Heterostructure Nanocomposite Electrolyte of $Ce_{0.8}Sm_{0.2}O_{2-\delta}$−$SrTiO_3$ for Low-Temperature Solid Oxide Fuel Cells. *Nano-Micro Lett.* **2021**, *13*, 1−14.

(43) Yousaf, M.; Mushtaq, N.; Zhu, B.; Wang, B.; Akhtar, M. N.; Noor, A.; Afzal, M. Electrochemical properties of $Ni_{0.4}Zn_{0.6}Fe_2O_4$ and the heterostructure composites (Ni−Zn ferrite-SDC) for low temperature solid oxide fuel cell (LT-SOFC). *Electrochim. Acta* **2020**, *331*, 135349.

(44) Aoki, M.; Chiang, Y.-M.; Kosacki, I.; Lee, L. J.-R.; Tuller, H.; Liu, Y. Solute segregation and grain-boundary impedance in high-purity stabilized zirconia. *J. Am. Ceram. Soc.* **1996**, *79*, 1169−1180.

(45) Xia, C.; Mi, Y.; Wang, B.; Lin, B.; Chen, G.; Zhu, B. Shaping triple-conducting semiconductor $BaCo_{0.4}Fe_{0.4}Zr_{0.1}Y_{0.1}O_{3-\delta}$ into an electrolyte for low-temperature solid oxide fuel cells. *Nat. Commun.* **2019**, *10*, 1−9.

(46) Shah, M. A. K. Y.; Zhu, B.; Rauf, S.; Mushtaq, N.; Yousaf, M.; Ali, N.; Tayyab, Z.; Akbar, N.; Yang, C. P.; Wang, B. Electrochemical Properties of a Co-Doped $SrSnO_{3-\delta}$-Based Semiconductor as an Electrolyte for Solid Oxide Fuel Cells. *ACS Appl. Energy Mater.* **2020**, *3*, 6323−6333.

(47) El-Fadl, A. A.; El-Maghraby, E.; Mohamad, G. Influence of gamma radiation on the absorption spectra and optical energy gap of Li-doped ZnO thin films. *Cryst. Res. Technol.* **2004**, *39*, 143−150.

(48) Li, Z. a.; Zhu, Z.; Chueh, C.-C.; Jo, S. B.; Luo, J.; Jang, S.-H.; Jen, A. K.-Y. Rational design of dipolar chromophore as an efficient dopant-free hole-transporting material for perovskite solar cells. *J. Am. Chem. Soc.* **2016**, *138*, 11833−11839.

(49) Luo, W.; Li, F.; Li, Q.; Wang, X.; Yang, W.; Zhou, L.; Mai, L. Heterostructured Bi_2S_3−Bi_2O_3 Nanosheets with a Built-In Electric Field for Improved Sodium Storage. *ACS Appl. Mater. Interfaces* **2018**, *10*, 7201−7207.

(50) Li, C.; Dong, S.; Tang, R.; Ge, X.; Zhang, Z.; Wang, C.; Lu, Y.; Yin, L. Heteroatomic interface engineering in MOF-derived carbon heterostructures with built-in electric-field effects for high performance Al-ion batteries. *Energy Environ. Sci.* **2018**, *11*, 3201−3211.

(51) Zheng, Y.; Zhou, T.; Zhao, X.; Pang, W. K.; Gao, H.; Li, S.; Zhou, Z.; Liu, H.; Guo, Z. Atomic Interface Engineering and Electric-Field Effect in Ultrathin Bi_2MoO_6 Nanosheets for Superior Lithium Ion Storage. *Adv. Mater.* **2017**, *29*, 1700396.

(52) Shao, K.; Li, F.; Zhang, G.; Zhang, Q.; Maliutina, K.; Fan, L. Approaching durable single-layer fuel cells: promotion of electroactivity and charge separation via nanoalloy redox exsolution. *ACS Appl. Mater. Interfaces* **2019**, *11*, 27924−27933.

(53) Liu, K.; Ganesh, K. S.; Nie, J.; He, Z.; Xia, C.; Dong, W.; Wang, X.; Wang, H.; Wang, B. Characterizing the Blocking Electron Ability of the Schottky Junction in SnO_2−SDC Semiconductor−Ionic Membrane Fuel Cells. *ACS Sustainable Chem. Eng.* **2020**, *8*, 10357−10368.

(54) Meng, Y.; Wang, X.; Zhang, W.; Xia, C.; Liu, Y.-n.; Yuan, M.; Zhu, B.; Ji, Y. Novel high ionic conductivity electrolyte membrane based on semiconductor $La_{0.65}Sr_{0.3}Ce_{0.05}Cr_{0.5}Fe_{0.5}O_{3-\delta}$ for low-temperature solid oxide fuel cells. *J. Power Sources* **2019**, *421*, 33−40.

https://doi.org/10.1021/acsaem.1c01186
ACS Appl. Energy Mater. 2021, 4, 8922−8932